An Integrated OTFS-NOMA Framework for Multi-Beam LEO Systems: Reliability and Capacity Analysis

Xiaohui Zhao, Lei Lei, *Senior Member, IEEE,* Zhiqiang Wei, *Member, IEEE,* Hai Fang, Wenjie Wang, *Senior Member, IEEE,* Symeon Chatzinotas, *Fellow, IEEE*

***Abstract*—Multi-beam low earth orbit (LEO) satellite communications, as an essential component for 6G systems, may encounter challenges from severe Doppler shifts and co-channel interference. This paper addresses a realistic problem in 6G-LEO systems, that is, how to meet the high-reliability demands of massive high-mobility terminals. We propose an integrated framework to exploit the synergy of non-orthogonal multiple access (NOMA) and orthogonal time frequency space (OTFS). OTFS modulation is employed to achieve full time-frequency diversity to combat Doppler shifts, while NOMA is used to accommodate more access requests. Specifically, within each beam, power domain superposition is applied to the delay-Doppler domain, enabling multiple terminals to share delay-Doppler grid resources. We analyze the performance of reliability, outage probability and ergodic capacity. Notably, we derive a novel closed-form expression to characterize the distribution of multi-beam interference with varying beam gains. Theoretical analysis and simulation results confirm that the proposed framework achieves a substantially lower outage probability compared to conventional OFDM schemes, with a system capacity improvement exceeding 11.9%.**

***Index Terms*—Low earth orbit satellite, OTFS, NOMA, performance analysis, outage probability.**

I. Introduction

High-throughput low earth orbit (LEO) satellites have emerged as an essential component for the future sixth generation (6G) system [1]. In the coming years, we expect the establishment of an integrated air-space-ground communication grid that will combine terrestrial cellular networks, satellite networks, high-altitude platforms, unmanned aerial vehicles (UAVs), and ocean-based machine-type communication networks. A defining feature of these future communication scenarios will be high mobility. Concurrently, the 6G communication framework has introduced enhanced performance benchmarks across application scenarios and transmission metrics. As we prepare for the proliferation of high-mobility environments, such as high-speed railways, vehicular networks, and massive machine-type communications on high-speed platforms, LEO satellites face several challenges. They must ensure low transmission delays and maintain high data rates in these dynamic settings [2].

The orthogonal frequency division multiplexing (OFDM) technology, due to its high spectral efficiency and low transceiver complexity, has been widely deployed in cellular networks, WiFi, and satellite communication systems [3]. However, OFDM has its inherent limitations in poor resistance to carrier frequency offset, high peak-to-average power ratio, and out-of-band power leakage, which make it unsuitable for space-based information networks in emerging scenarios. In general, low-speed terminals equipped with Doppler shift (DS) estimators can use satellite ephemeris and their location data to estimate and compensate for DSs caused by satellite movement. However, this DS estimation process consumes additional resources, which is challenging for resource-limited devices. Moreover, for high-mobility terminals with rapidly varying positions and unknown motion dynamics, tracking and compensating for DSs, caused by relative high-speed movement between the transmitter and receiver, becomes even more difficult. This makes conventional waveforms less effective in such scenarios.

To address the challenge of reliable data transmission in high-mobility environments, the orthogonal time-frequency space (OTFS) modulation is proposed to exploit the slow channel variations in the delay-Doppler (DD) domain, providing robust resistance against the time-selective fading caused by DSs [4]. The modulation symbols in the DD domain are spread across the entire time-frequency (TF) domain, thereby achieving diversity gain. Compared to conventional OFDM, OTFS is more suitable for high-mobility scenarios, offering enhanced performance in dynamic environments.

A. Related Works

In recent years, the majority of the OTFS works concentrated on channel estimation, signal detection, and multiple access

This work was supported in part by the National Natural Science Foundation of China (NSFC) project under Grant 62471375; in part by the Natural Science Foundation of Sichuan Province, China, under Grant 2023NSFSC0455; in part by the National Key Laboratory Foundation under Grant 2023-JCJQ-LB-007, in part by the Qin Chuangyuan Innovation and Talent Project under Grant QCYRCXM-2023-049, and in part by the Key Research and Development Program of Shaanxi under Grant 2024GX-YBXM-065.

Xiaohui Zhao, Lei Lei, Wenjie Wang are with the School of Information and Communications Engineering, Xi'an Jiaotong University, Xi'an 710049, China (e-mail: xhzhao@stu.xjtu.edu.cn; lei.lei@xjtu.edu.cn; wjwang@mail.xjtu.edu.cn).

Zhiqiang Wei is with the School of Mathematics and Statistics, Xi'an Jiaotong University, Xi'an 710049, China, also with the Peng Cheng Laboratory, Shenzhen, Guangdong 518055, China, and also with the Pazhou Laboratory (Huangpu), Guangzhou, Guangdong 510555, China (e-mail: zhiqiang.wei@xjtu.edu.cn).

Hai Fang is with the Xi'an Institute of Space Radio Technology, Xi'an 710100, China (e-mail: hai_fang@yeah.net).

Symeon Chatzinotas is with the Interdisciplinary Center for Security, Reliability and Trust, University of Luxembourg, 1855 Esch-sur-Alzette, Luxembourg (e-mail: symeon.chatzinotas@uni.lu).

techniques in terrestrial networks [5]–[10]. In [5], the Zak transform of time domain signals was employed to derive the implementation of OTFS, elucidating the inherent robustness of DD domain modulation against Doppler shift induced by the channel. Studies in [6] introduced a channel estimation and symbol detection framework based on superimposed pilots, where pilots are overlaid onto data symbols without compromising spectral efficiency. Liu et al. [7] developed an expectation-maximization variational Bayes algorithm for estimating uplink channel parameters. Furthermore, [8]–[10] cover the principles of OTFS modulation, transmitter and receiver setup, and extending OTFS applications to integrated sensing and communication. However, satellite communications face severe DSs, which OTFS is well-positioned to address.

Research on the application of OTFS technology to LEO satellite communication is still in its exploratory phase. In [11], a review is presented discussing the feasibility and advantages of applying OTFS to LEO satellite communication, along with detection schemes based on the DD domain and a set of promising research directions. In [12], an OTFS-based joint channel estimation and data detection algorithm was proposed, where variational Bayesian inference was employed to estimate the layered channel vector. Meanwhlie, the unknown data symbols were leveraged to provide additional measurement information, improving the estimation and decoding performance. In response to large-scale carrier frequency offset (CFO) in satellite systems, [13] introduced an OTFS-based CFO estimator that inserts pilot signals and maximum length sequences in the DD domain. In [14], the downlink performance of LEO satellites operating at millimeter-wave frequencies was evaluated. The results show that OTFS exhibits high robustness to DSs in any channel.

In the integrated satellite-terrestrial network, the introduction of terrestrial or low-altitude relays can effectively enhance the overall performance of communication systems. Hu et al. [15] explored the security performance of the uplink in LEO satellite augmented by UAV collaboration. OTFS is utilized to mitigate the significant DSs caused by high mobility, and the secure outage probability (OP) at the legitimate receiver is derived. For the downlink communications, the study in [16] investigates the use of UAV collaboration to compensate for the path loss caused by long-distance transmission of OTFS signals. The research derived a closed-form OP expression and established conditions for UAV cooperation that ensure a positive reliability gain. To extend communication coverage, [17] proposed the introduction of a reconfigurable intelligent surface in the space-air-ground system. It adjusts the phase shifts of the reconfigurable intelligent surface based on statistical channel state information in the DD domain, to maximize the line-of-sight (LoS) power at the destination. However, the introduction of relays naturally increases system overhead. In particular, in scenarios with massive terminals, extensive feedback information may overwhelm the relays.

On the other hand, given the limited spectrum resources and the massive access requirements, satellites with OTFS modulation often prefer non-orthogonal multiple access (NOMA) technologies to achieve efficient data access. To enable both stationary and mobile terminals to multiplex TF resources, an OTFS-NOMA scheme for terrestrial networks was proposed in [18], and an efficient receiver was designed. Moreover, by integrating the grant-free NOMA paradigm of satellites with OTFS, Zhou et al. [19] proposed a two-stage successive active terminal identification and channel estimation scheme for multi-terminal transmission, to accommodate massive IoT access. This scheme reduces long-term round-trip delays, and mitigates the impact of DSs in satellite links. In LEO satellite scenarios serving massive machine type communication, a differential DS-based OTFS-tandem spreading multiple access scheme was proposed in [20]. This scheme introduces a differential Doppler resource allocation scheme that optimizes coverage area and access point distribution, effectively mitigating data conflicts in massive uplink transmissions. However, existing schemes have not yet considered the impact of inter-beam interference, and the performance of OTFS combined with multiple access requires further investigation.

B. Contributions

Overall, most recent LEO-OTFS works focus on single beam scenarios [15]–[18], with limited analysis on multi-beam configurations. In practice, fixed-beam antennas are insufficient to meet the demands of 6G networks. The majority of LEO satellites has transitioned to phased array multi-beam antennas, which more effectively utilize spatiotemporal resources, and enhance service quality. It is essential to investigate OTFS performance in such multi-beam configurations. This paper investigates an integrated OTFS-NOMA framework for multi-beam LEO downlink communication systems serving massive high-mobility terminals. The contributions of this paper are as follows:

- We propose an efficient OTFS-NOMA framework to support reliable communications for high-mobility terminals. In the framework, the served terminals in each time slot share the full DD domain resources to enable significant mitigation of DSs, while NOMA is introduced to support massive terminals and enhance system capacity.
- We develop a downlink transmission model for OTFS-NOMA signals, and derive closed-form expressions for the OP and ergodic capacity. Specifically, we derive a new expression to characterize the distribution of the sum of multi-beam interference with different gains. This expression has a simple finite-sum form, avoiding the complexity of special functions and infinite series in conventional expressions. The expression can be generalized for the analysis of most multi-beam LEO scenarios.
- We provide a systematic evaluation to show how the transmission signal-to-noise ratio, inter-beam interference, intra-beam interference, DD domain parameters, and frequency offset estimation bias affect the performance of OP, bit error rate, ergodic capacity for the proposed integrated OTFS-NOMA framework in multi-beam LEO systems. The results show that the proposed framework achieves a lower OP compared to the comparison schemes, and increases system capacity by more than 11.9%.

II. System Model

A. The Satellite-to-Ground Link Model

Consider a typical scenario of a multi-beam LEO downlink communication system, serving massive high-mobility terminals, as shown in Figure 1. The satellite is equipped with multiple terminal link antennas in the Ku-band [11]. The terminal link antennas consist of multiple phased arrays, which, through a power-division network, generate U spot beams for downlink communication, indexed as $u = 1, 2, ..., U$. Each spot beam covers a distinct area on the ground, forming a cell, and provides communication services to high-mobility ground terminals equipped with single directional antenna. We assume that the receiving antennas can effectively track and align with the transmitted beams.

The long transmission distances and significant signal attenuation associated with LEO satellites necessitate the use of multiple transmit antennas to generate beams, thereby enhancing transmission performance. Additionally, the high relative speed between the satellite and the terminals induces substantial DSs. OTFS modulation counters this by achieving full TF diversity, modulating the signal in the DD domain.

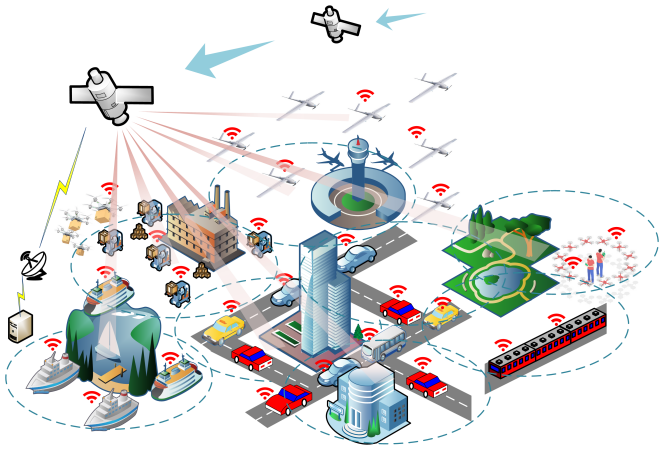

Fig. 1. A multi-beam LEO scenario with high-mobility terminals.

Considering a TF dual-dispersive channel, the extension function of DD domain is denoted by

$$h(\tau, \nu) = \sum_{p=1}^{L} h_p \delta(\tau - \tau_p)\, \delta(\nu - \nu_p), \tag{1}$$

where L denotes the number of propagation paths, p is its index, and h_p, τ and ν denote the channel gain, delay, and DS, respectively.

Define the OTFS system transmission bandwidth as $B = M\Delta f$, and the transmission duration as $T_s = NT$, where M and N represent the number of discrete points in frequency and time domain, respectively. Here, Δf and T are the frequency and time domain sampling interval, respectively, which determine the maximum delay $\tau_{\max} < T$ and maximum DS $\nu_{\max} < \Delta f/2$ that the system can support. The delay and DS of the p-th path can be given by $\tau_p = \frac{l_p + l'_p}{M\Delta f}$ and $\nu_p = \frac{k_p + k'_p}{NT}$, where $l_p \in [0, M-1]$ and $k_p \in [0, N-1]$ are the integer indexes of delay tap and DS tap, and l'_p and k'_p are the corresponding non-integer multiple offsets. Therefore, increasing M and N can improve the DD domain resolution, and reduce the performance degradation caused by the fractional DS and delay. However, it leads to adverse effects such as higher system complexity and larger peak-to-average power ratio.

Moreover, assuming that the satellite-to-ground channel follows the shadowed rice (SR) distribution [21], the probability density function (PDF) of the channel fading amplitude envelope from the i-th antenna to the j-th terminal is derived as

$$f_{h_{j,i}}(x) = \alpha_{j,i} x e^{-\beta_{j,i} x^2}\, {}_1F_1\left(\eta_{j,i}; 1; c_{j,i} x^2\right), \forall x \geq 0, \tag{2}$$

where $\alpha_{j,i} \triangleq \left(\frac{2b_{j,i}\eta_{j,i}}{2b_{j,i}\eta_{j,i}+\omega_{j,i}}\right)^{\eta_{j,i}} / b_{j,i}$, $\beta_{j,i} \triangleq 1/2b_{j,i}$, $c_{j,i} \triangleq \omega_{j,i}/\left(2b_{j,i}\left(2b_{j,i}\eta_{j,i} + \omega_{j,i}\right)\right)$, and ${}_1F_1(.;.;.)$ is the Kummer confluent hypergeometric function. The parameters $\omega_{j,i}$, $2b_{j,i}$ and $\eta_{j,i}$ represent the average power of the LoS path component, the average power of the non line-of-sight (NLoS) path component and the Nakagami parameter, respectively, for the satellite-to-ground channel of the transmit antenna i to terminal j.

B. The DD Domain Channel Model of the OTFS

For the OTFS system, its input-output relationship is expressed as

$$y[k,l] = \sum_{p=1}^{L} h_p e^{-j2\pi\tau_p\nu_p} x\left[[k-k_p]_N, [l-l_p]_M\right] + z[k,l], \tag{3}$$

where x, y, and z represent the modulation symbols, demodulation symbols, and noise in the DD domain, respectively, and $[.]_N$ denotes the modulo N operation. Its matrix form is expressed as $\mathbf{y} = \mathbf{H}\mathbf{x} + \mathbf{z}$. The DD domain equivalent channel matrix $\mathbf{H} \in \mathbf{C}^{MN \times MN}$ is denoted as

$$\mathbf{H} = \left(\mathbf{F_N} \otimes \mathbf{G_{rx}}\right) \sum_{p=1}^{L} h_p \mathbf{\Xi}^{l_p} \mathbf{\Phi}^{k_p} \left(\mathbf{F_N^H} \otimes \mathbf{G_{tx}}\right), \tag{4}$$

where $\mathbf{\Xi}^{l_p} \in \mathbf{C}^{MN \times MN}$ is the cyclic shift matrix, which implements the multiplied matrix to loop l_p times from top to bottom in row. The matrix

$$\mathbf{\Phi}^{k_p} = \text{diag}\left(\left[1, e^{j2\pi k_p/MN}, ..., e^{j2\pi k_p(MN-1)/MN}\right]\right) \tag{5}$$

is the diagonal matrix containing MN roots. $\mathbf{F_N} \in \mathbf{C}^{N \times N}$ is the N-point DFT matrix. $\mathbf{G_{tx}}$ and $\mathbf{G_{rx}}$ are diagonal matrices, with sampled transmitting pulse $g_{tx}(t)|_{t=mT/M}$ and receiving pulse $g_{rx}(t)|_{t=mT/M}$ as the main diagonal elements, respectively.

To be specific, $\mathbf{H}$ is a block circulant matrix with circulant blocks. For example, assuming $N = 5$ and $M = 4$, the channel matrix of terminal q is shown in Figure (2a). The DD domain equivalent channel can be regarded as $N \times N$ blocks, each of which is $M \times M$.

Based on the main block-diagonal, the degree of left or right shift is determined by the integer DS of each path. For example, the third path with $k_3 = 2$ shifts the main block-diagonal by two block lengths to the left, while the fourth path

with $k_4 = -2$ shifts the main diagonal by two block lengths to the right. In addition, the delay parameter of each path causes the rows in the sub-block to undergo the same permutation. For the first path with $l_1 = 0$, the non-zero elements of each sub-blocks are placed in the main diagonal. However, for the second path with $l_2 = 1$, the last row of each sub-block loops to the first row. On the other hand, the DD domain equivalent channel with fractional DSs is shown in Figure (2b). It can be seen that fractional DSs cause energy leakage into each Doppler component. Most of the energy is concentrated in the region of shift $[k_p]_{\text{round}}$, while the remaining energy is dispersed to varying degrees within each block, where $[.]_{\text{round}}$ is the nearest integer.

Fractional DSs will cause Doppler interference. The interference intensity depends on the difference between the fractional part and 0.5, i.e., the closer the fractional part is to 0.5, the more energy is diffused, and vice versa, as shown in Figure (2b), where the energy spread of the third path is larger than that of the second path. In summary, the OTFS waveform can be resolved in the DD domain when the DS is an integer. However, due to the the limited Doppler resolution in practical communication, it is easy to cause Doppler interference. By increasing the signal duration, the interference can be effectively reduced. The effect of fractional DSs on OTFS is explained more in Section V below.

III. An Integrated OTFS-NOMA Framework

In order to overcome the DSs, OTFS modulation is used to resist the performance degradation. In addition, for the service requests of the massive terminals, the NOMA technology is introduced in each beam to increase the transmission rate.

Suppose there are C_u high-mobility terminals requesting traffic service in the region covered by the u-th beam of LEO. First, through the terminal selection algorithm [22], J_u terminals in beam u are selected to form a group at the current time slot. Next, the terminals within a group share the DD domain resources, and the transmission complex baseband symbols are superimposed in the $M \times N$ DD domain grid, represented as $x_u[k,l] = \sum_{j=1}^{J_u} \sqrt{\xi_{j^u}} s_{j^u}[k,l]$, where $s_{j^u}\left(E\left[|s|^2\right]=1\right)$ and ξ_{j^u} are the transmission symbols and the NOMA power allocation coefficients of terminal j, respectively. Assume that the total power is fully allocated to the terminals, i.e., $\sum_{j=1}^{J_u} \xi_{j^u} = 1$.

Subsequently, the symbols in DD domain are transformed to TF domain by inverse symplectic finite Fourier transform, which can be given by

$$X_u[\kappa,\iota] = \frac{\sqrt{P_u}}{NM} \sum_{k=0}^{N-1} \sum_{l=0}^{M-1} x_u[k,l]\, e^{j2\pi\left(\frac{\kappa k}{N} - \frac{\iota l}{M}\right)}, \quad (6)$$

where P_u is the transmission power of the signal, $0 \le \kappa \le N-1$ and $0 \le \iota \le M-1$ are two-dimensional indexes in TF domain. Utilizing the Heisenberg transform, X_u is converted into a time-delay domain signal, and adding a cyclic prefix. Through digital analog conversion, the continuous analog signal is transmitted through antenna $i, 1 \leqslant i \leqslant N_u$.

At the receiver, applying Wigner transform, the TF domain sampling signal of q-th terminal in m-th beam is given by

$$Y_{q^m}[\kappa,\iota] = \sum_{u=1}^{U} \sqrt{G_u} \sum_{i=1}^{N_u} H_{q^m,i^u}[\kappa,\iota]\, X_u[\kappa,\iota] + Z_{q^m}[\kappa,\iota], \quad (7)$$

where $G_u \triangleq G(\theta_{m,u})$ is the beam gain [23, Eq. (3)], and $\theta_{m,u}$ is the nadir angle between m-th beam coverage center position and u-th beam center position with respect to the satellite. $H_{q^m,i^u}[\kappa,\iota]$ is the TF domain equivalent channel from the i-th transmit antenna in beam u to the q-th terminal's receive antenna in beam m. It can be obtained from the channel response, which can be given by

$$H_{q^m,i^u}[\kappa,\iota] = \int\int h_{q^m,i^u}(\tau,v)\, e^{j2\pi(vnT - \tau(v+m\Delta f))} dv d\tau. \quad (8)$$

$Z_{q^m}[\kappa,\iota]$ is the complex Gaussian distributed noise at the filter output. Finally, the symplectic finite Fourier transform is applied to sampling signal to obtain the DD domain estimates symbols, which is given by

$$y_{q^m}[k,l] = \frac{1}{NM} \sum_{\kappa=0}^{N-1} \sum_{\iota=0}^{M-1} Y_{q^m}[\kappa,\iota]\, e^{-j2\pi\left(\frac{\kappa k}{N} - \frac{\iota l}{M}\right)}. \quad (9)$$

According to the input-output relationship in the DD domain, the matrix form of the signal model in the DD domain is as follows,

$$\mathbf{y}_{q^m} = \sum_{u=1}^{U} \sqrt{P_u G_u} \sum_{i=1}^{N_u} \mathbf{H}_{q^m,i^u} \mathbf{x}_u + \mathbf{z}_{q^m}, \quad (10)$$

where $\mathbf{x}, \mathbf{y}, \mathbf{z} \in \mathbf{C}^{MN\times 1}$ are the sending symbols vector, the receiving signals vector, and the noise vector in the DD domain, respectively. The $(k+Nl+1)$-th element of vector $\mathbf{x}_u$ is $x_u[k,l]$, and the same goes for $\mathbf{y}$ and $\mathbf{z}$.

The DD domain estimated symbol is given by

$$\begin{aligned}\mathbf{y}_{q^m} = & \underbrace{\sqrt{P_m G_m} \sum_{i=1}^{N_m} \mathbf{H}_{q^m,i^m} \sqrt{\xi_{q^m}} \mathbf{s}_{q^m}}_{\text{the desired signal}} \\ & + \underbrace{\sqrt{P_m G_m} \sum_{i=1}^{N_m} \sum_{j=q+1}^{J_m} \mathbf{H}_{q^m,i^m} \sqrt{\xi_{j^m}} \mathbf{s}_{j^m}}_{\text{intra-beam interference}} \\ & + \underbrace{\sum_{\substack{u=1 \\ u\neq m}}^{U} \sqrt{P_u G_u} \sum_{i=1}^{N_u} \mathbf{H}_{q^m,i^u} \sum_{j=1}^{J_u} \sqrt{\xi_{j^u}} \mathbf{s}_{j^u}}_{\text{inter-beam interference}} + \mathbf{z}_{q^m},\end{aligned} \quad (11)$$

where $\mathbf{s} \in \mathbf{C}^{MN\times 1}$ is the symbol vector transmitted to the terminal. The first term is the desired information of terminal q in beam m. The second term is the intra-beam interference caused by other terminal signals in beam m. To be specific, assuming that the terminal's NOMA coefficients are arranged as $\xi_1 > \cdots > \xi_{J^m}$ in beam m, based on perfect successive interference cancellation, the estimates symbols of terminal q is only interfered by signals from $J-q$ terminals instead of J. The third term is the inter-beam interference caused by

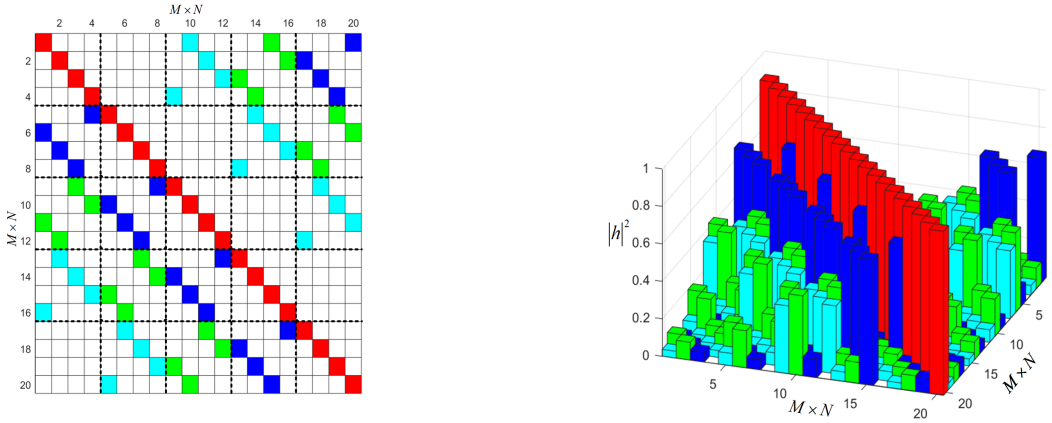

(a) The channel parameters $l_p = \{0, 1, 2, 3\}$, $k_p = \{0, 1, 2, -2\}$.

(b) The channel parameters $l_p = \{0, 1, 2, 3\}$, $k_p = \{0, 1.125, 2.312, -2.851\}$.

Fig. 2. The DD domain equivalent channel with (a) integer DSs, and (b) fractional DSs.

signals from other beams to beam m. The last term is the complex Gaussian noise in the DD domain, which follows the distribution $\mathcal{CN}\left(0, \sigma_{q^m}^2\right)$.

Due to the block-cyclic structure of $\mathbf{H}$, the inter-symbol interference still exists at the receiver, as is also evident from (3). Therefore, equalization techniques are required at the receiver to mitigate inter-symbol interference. We apply the frequency domain zero-forcing linear equalizer to process the received signal in the DD domain. This process can be represented as the multiplication of the signal matrix and the equalization matrix $\mathbf{Q}_{q^m,m}$, which can be given by

$$\begin{aligned}&\mathbf{Q}_{q^m,m}\mathbf{y}_{q^m} = \\ &\sqrt{P_m G_m}\sqrt{\xi_{q^m}}\mathbf{s}_{q^m} + \sqrt{P_m G_m}\sum_{j=q+1}^{J_m}\sqrt{\xi_{j^m}}\mathbf{s}_{j^m} \\ &+\mathbf{Q}_{q^m,m}\sum_{\substack{u=1\\u\neq m}}^{U}\sqrt{P_u G_u}\sum_{i=1}^{N_u}\mathbf{H}_{q^m,i^u}\sum_{j=1}^{J_u}\sqrt{\xi_{j^u}}\mathbf{s}_{j^u} \\ &+\mathbf{Q}_{q^m,m}\mathbf{z}_{q^m}\end{aligned}, \tag{12}$$

where $\mathbf{Q}_{q^m,m} = \left(\mathbf{F}_N^H \otimes \mathbf{F}_M\right)\mathbf{A}_{q^m,m}^{-1}\left(\mathbf{F}_N \otimes \mathbf{F}_M^H\right)$, $\left(\mathbf{F}_N \otimes \mathbf{F}_M^H\right)\mathbf{y}_{q^m}$ represents the transformation of the received signal from the DD domain to the TF domain. As a result, the channel matrix at the terminal can be diagonalized, resulting in a diagonal matrix $\mathbf{A}_{q^m,m}$, where the $(\kappa M + \iota + 1)$-th diagonal element is $A_{q^m,m}^{\kappa,\iota} = \sum_{k=0}^{N-1}\sum_{l=0}^{M-1} a_{k,q^m,m}^{l,1} e^{j2\pi\left(\frac{l\iota}{M} - \frac{k\kappa}{N}\right)}$, $a_{k,q^m,m}^{l,1}$ is the $(kM + l + 1)$-th row and the first column of the matrix $\sum_{i=1}^{N_m}\mathbf{H}_{q^m,i^m}$. Additionally, $\left(\mathbf{F}_N \otimes \mathbf{F}_M^H\right)$ is a unitary matrix, i.e., $\left(\mathbf{F}_N \otimes \mathbf{F}_M^H\right)^{-1} = \left(\mathbf{F}_N^H \otimes \mathbf{F}_M\right)$.

Furthermore, in order to obtain the signal-to-interference-and-noise ratio (SINR) of the equalized signal, the covariance matrices of the inter-beam interference term and noise term need to be calculated. For the inter-beam interference term, the covariance matrix is given by (13), at the top of next page. Here, both $\mathbf{A}_{q^m,u}$ and $\mathbf{A}_{q^m,m}$ are diagonal matrices. Therefore, C_{cov} is a block-circulant matrix whose eigenvalues I_{ibi} can be given by its trace, i.e.,

$$\begin{aligned}I_{ibi} &= \tfrac{1}{MN}\mathrm{Tr}\left\{\mathbf{A}_{q^m,m}^{-2}\left(\sum_{\substack{u=1\\u\neq m}}^{U}P_u G_u \mathbf{A}_{q^m,u}\right)^2\right\} \\ &= \tfrac{1}{MN}\sum_{\kappa'=0}^{N-1}\sum_{\iota'=0}^{M-1}\left|\sum_{i=1}^{N_m}A_{q^m,i^m}^{\kappa',\iota'}\right|^{-2}\underbrace{\left|\sum_{\substack{u=1\\u\neq m}}^{U}P_u G_u\sum_{i=1}^{N_u}A_{q^m,i^u}^{\kappa',\iota'}\right|^2}_{\triangleq\Psi(\kappa',\iota')},\end{aligned} \tag{14}$$

where $\mathrm{Tr}\{.\}$ is the trace of the matrix. Similarly, the eigenvalues I_n of the covariance matrix of the noise term can also be given by

$$\begin{aligned}I_n &= \frac{1}{MN}\mathrm{Tr}\left\{\mathbf{A}_{q^m,m}^{-1}\mathbf{A}_{q^m,m}^{-H}\right\} \\ &= \frac{\varepsilon}{MN}\sum_{\kappa'=0}^{N-1}\sum_{\iota'=0}^{M-1}\underbrace{\left|\sum_{i=1}^{N_m}A_{q^m,i^m}^{\kappa',\iota'}\right|^{-2}}_{\triangleq\Xi(\kappa',\iota')},\end{aligned} \tag{15}$$

where $\varepsilon = \sigma_{q^m}^2$. Therefore, the SINR of decoding the estimated symbol $s_{q^m}[k,l]$ is given by

$$\mathrm{SINR}_{q^m} = \frac{P_m G_m \xi_{q^m}}{P_m G_m\sum_{j=q+1}^{J_m}\xi_{j^m} + I_{ibi} + I_n}. \tag{16}$$

IV. PERFORMANCE ANALYSIS

A. Outage Probability Analysis

The OP is defined as the probability that the data rate is less than a certain threshold γ, such that

$$P(\gamma) \triangleq \Pr\{R \leq \gamma\}. \tag{17}$$

Therefore, the OP of terminal q in beam m is given by

$$P\left(\gamma_{q^m}\right) = \Pr\left\{\sum_{\kappa'=0}^{N-1}\sum_{\iota'=0}^{M-1}\underbrace{\Xi\left(\kappa',\iota'\right)\left(\Psi\left(\kappa',\iota'\right)+\varepsilon\right)}_{\triangleq\chi} \geq \varsigma_{q^m}\right\}, \tag{18}$$

$$
\begin{aligned}
&C_{cov} = \\
&E\left\{\left(\mathbf{F}_N^{\mathrm{H}} \otimes \mathbf{F}_M\right) \mathbf{A}_{q^m,m}^{-1} \left(\mathbf{F}_N \otimes \mathbf{F}_M^H\right) \sum_{\substack{u=1 \\ u\neq m}}^{U} P_u G_u \mathbf{H}_{q^m,u} \left(\sum_{\substack{u=1 \\ u\neq m}}^{U} P_u G_u \mathbf{H}_{q^m,u}\right)^{\mathrm{H}} \left(\mathbf{F}_N^{\mathrm{H}} \otimes \mathbf{F}_M\right) \mathbf{A}_{q^m,m}^{-\mathrm{H}} \left(\mathbf{F}_N \otimes \mathbf{F}_M^{\mathrm{H}}\right)\right\} \\
&= \left(\mathbf{F}_N^{\mathrm{H}} \otimes \mathbf{F}_M\right) \mathbf{A}_{q^m,m}^{-1} \sum_{\substack{u=1 \\ u\neq m}}^{U} P_u G_u \mathbf{A}_{q^m,u} \left(\sum_{\substack{u=1 \\ u\neq m}}^{U} P_u G_u \mathbf{A}_{q^m,u}\right)^{\mathrm{H}} \mathbf{A}_{q^m,m}^{-\mathrm{H}} \left(\mathbf{F}_N \otimes \mathbf{F}_M^{\mathrm{H}}\right)
\end{aligned} \tag{13}
$$

where

$$
\varsigma_{q^m} = \frac{MNP_m G_m \left(\sum_{j=q}^{J_m} \xi_{j^m} - 2^{\gamma_{q^m}} \sum_{j=q+1}^{J_m} \xi_{j^m}\right)}{2^{\gamma_{q^m}} - 1}. \tag{19}
$$

Obviously, the OP is always one when ς_{q^m} is less than zero. Therefore, the power allocation coefficients should be set to satisfy $\sum_{j=q}^{J_m} \xi_{j^m} > 2^{\gamma_{q^m}} \sum_{j=q+1}^{J_m} \xi_{j^m}$ for successful NOMA implement. At the same time, when the threshold γ increases, ς in (18) will decrease, so the OP will increase while χ remains constant, which is the same as the actual law in engineering.

First, the PDF of random variables (RVs) Ξ and Ψ are analyzed separately. For notational convenience, the q^m-th, i-th, and κ', ι' indexes are dropped. Since the RV A_{i^u} follows the SR distribution, i.e., $A_{i^u} \sim SR\left(b_{i^u}, \omega_{i^u}, \eta_{i^u}\right)$. Define RV $X_u' \triangleq \sum_{i=1}^{N_u} A_{i^u}$ to be the sum of N_u non-i.i.d. SR distributions RVs. Due to satellite channel characteristics, the signals of N_u transmitting antennas pass through approximately the same channel. Therefore, N_u RVs can be represented linearly with each other. For example, suppose $A_{1^u} \sim SR\left(b_{1^u}, \omega_{1^u}, \eta_{1^u}\right)$, $A_{2^u} = kA_{1^u}, k > 0$, and $A_{2^u} \sim SR\left(b_{2^u} = k^2 b_{1^u}, \omega_{2^u} = k^2 \omega_{1^u}, \eta_{2^u} = \eta_{1^u}\right)$. See Appendix A for the proof. This conclusion shows the relationship of linearly dependent SR distributions. When A_{2^u} is scaled k times based on A_{1^u}, the average power of LOS and NLOS path component of A_{2^u} are scaled k^2 times compared to that of A_{1^u}, while the fading parameters remain the same.

Furthermore, the sum of N_u dependent SR distributions is still the SR distribution, and the PDF of X_u' can be given by

$$
f_{X_u'}(x) = f_{|h|}\left(x | \bar{b}_u, \bar{\omega}_u, \bar{\eta}_u\right), \tag{20}
$$

where $\bar{b}_u = \sum_{i=1}^{N_u} b_{i^u}$, $\bar{\omega}_u = \sum_{i=1}^{N_u} \omega_{i^u}$ and $\bar{\eta}_u = \eta_{i^u}, \forall i$. In addition, confluent hypergeometric function can be expressed as a sum of finite terms by [24, Eq. (9)], i.e., ${}_1F_1\left(\eta, 1, cx^2\right) = \sum_{k=0}^{\eta-1} \frac{c^k(\eta-1)!}{(\eta-1-k)!(k!)^2} x^{2k} e^{cx^2}$, where η is a strictly positive integer. Therefore, utilizing the derivative method of the distribution function, the PDF of Ξ can be given by

$$
\begin{aligned}
f_{\Xi}(x) &= \frac{1}{2} x^{-\frac{3}{2}} f_{X_m}\left(\frac{1}{\sqrt{x}}\right) \\
&= \frac{1}{2} \sum_{k_0=0}^{\eta_m-1} \alpha_m \xi_m(k_0)\, x^{-k_0-2} e^{-(\beta_m - c_m)x^{-1}},
\end{aligned} \tag{21}
$$

where $\xi_m(k_0) = \frac{c_m^{k_0}(\eta_m-1)!}{(\eta_m-1-k_0)!(k_0!)^2}$ is the coefficient.

For interference signals from ϖ ($\triangleq U-1$) beams, define $Y_u \triangleq \rho_u X_u'$, where $\rho_u = P_u G_u$, $u \neq m$. The PDF representation of Y_u is $f_{Y_u}(x) = \frac{1}{\rho_u} f_{X_u'}\left(\frac{x}{\rho_u}\right)$. Let RV $Z \triangleq Y_1 + Y_2 + \ldots Y_\varpi$ be the sum of ϖ i.i.d. RVs Y_u. The PDF of Z can be given in closed formulation by

$$
\begin{aligned}
f_Z(x) = &\sum_{k_1=0}^{\eta_1-1} \ldots \sum_{k_\varpi=0}^{\eta_\varpi-1} \Theta(\varpi) \sum_{r_2=0}^{2k_2-1} \ldots \sum_{r_\varpi=0}^{2k_\varpi-1} \Omega(\varpi) \\
&\sum_{v_2=0}^{\lfloor \Lambda_2/2 \rfloor} \ldots \sum_{v_\varpi=0}^{\lfloor \Lambda_\varpi/2 \rfloor} \Phi(\varpi)\, x^{\Lambda_\varpi + 2k_\varpi - 2v_\varpi + 1} e^{-\theta_\varpi x^2},
\end{aligned} \tag{22}
$$

where the parameters are defined as follows,

$$
\Theta(\varpi) = \prod_{i=1}^{\varpi} \alpha_i \xi_i(k_i)\, \rho_i^{-2k_i-2},
$$

$$
\Omega(\varpi) = \prod_{j=2}^{\varpi} \binom{2k_j+1}{r_j} (-1)^{r_j},
$$

$$
\Phi(\varpi) = \prod_{g=2}^{\varpi} \frac{\sqrt{\pi} \Lambda_g! \mu_g^{\Lambda_g - 2v_g} (\theta_{g-1} + \mu_g)^{v_g - \Lambda_g - \frac{1}{2}}}{4^{v_g} (\Lambda_g - 2v_g)! v_g!},
$$

and $\mu_g = \frac{\beta_g - c_g}{\rho_g^2}$, $\Lambda_g = \left(2\sum_{i=1}^{g-1} k_i - v_i\right) + r_g + g - 1$, $\theta_g = \mu_g - \frac{\mu_g^2}{\theta_{g-1} + \mu_g}$. The power exponent parameter θ_g iterates continuously as ϖ increases, assuming its initial value $\theta_1 = \mu_1$. When $\varpi = 1$, (22) degenerates into f_{Y_1}. See Appendix B for the proof. This closed-form expression is new in the analysis of multiple beams, although it has multiple summation terms, most of it has constant values and the independent variables have a simple structure.

Following this line of reasoning, the PDF of $\Psi + \varepsilon$ is obtained as $f_{\Psi+\varepsilon}(y) = \frac{f_Z\left(\sqrt{y-\varepsilon}\right)}{2\sqrt{y-\varepsilon}}$, which can be further written as

$$
\begin{aligned}
f_{\Psi+\varepsilon}(y) = &\sum_{k_1=0}^{\eta_1-1} \ldots \sum_{k_\varpi=0}^{\eta_\varpi-1} \Theta(\varpi) \sum_{r_2=0}^{2k_2-1} \ldots \sum_{r_\varpi=0}^{2k_\varpi-1} \Omega(\varpi) \\
&\sum_{v_2=0}^{\lfloor \Lambda_2/2 \rfloor} \ldots \sum_{v_\varpi=0}^{\lfloor \Lambda_\varpi/2 \rfloor} \frac{\Phi(\varpi)}{2} (y-\varepsilon)^{\frac{\Lambda_\varpi + 2k_\varpi - 2v_\varpi}{2}} e^{-\theta_\varpi (y-\varepsilon)}.
\end{aligned} \tag{23}
$$

The PDF of χ can be given by (24), at the top of next page, where $W_{a,b}(.)$ is Whittaker's W hypergeometric function. See Appendix C for the proof. Considering the distribution of the sum of MN times of RVs χ, it is very tricky. Therefore, the method of moment matching is employed to calculate the PDF. Now, derive the n-th order moment of χ, which can given by (25), at the top of next page, where $k_0 \geqslant n + r_0 + k_\varpi + 1$. See Appendix D for the proof.

$$f_{\chi}(z)=\sum_{k_0=0}^{\eta_m-1}\alpha_m\xi_m(k_0)\sum_{k_1=0}^{\eta_1-1}...\sum_{k_{\varpi}=0}^{\eta_{\varpi}-1}\Theta(\varpi)\sum_{r_2=0}^{2k_2-1}...\sum_{r_{\varpi}=0}^{2k_{\varpi}-1}\Omega(\varpi)\sum_{v_2=0}^{\lfloor\Lambda_2/2\rfloor}...\sum_{v_{\varpi}=0}^{\lfloor\Lambda_{\varpi}/2\rfloor}\Phi(\varpi)\frac{\varepsilon^{\frac{\Lambda_{\varpi}+2k_{\varpi}+2k_0-2v_{\varpi}+2}{4}}}{4z^{k_0+2}}$$
$$\frac{\Gamma\left(\frac{1}{2}\Lambda_{\varpi}+k_{\varpi}-v_{\varpi}+1\right)}{\left(\frac{\beta_m-c_m}{z}+\theta_{\varpi}\right)^{\frac{\Lambda_{\varpi}+2k_{\varpi}+2k_0-2v_{\varpi}+6}{4}}}e^{-\frac{\left(\frac{\beta_m-c_m}{z}+\theta_{\varpi}\right)\varepsilon}{2}+\theta_{\varpi}\varepsilon}W_{\frac{2k_0-\Lambda_{\varpi}-2k_{\varpi}+2v_{\varpi}+2}{4},-\frac{2k_0+\Lambda_{\varpi}+2k_{\varpi}-2v_{\varpi}+4}{4}}\left(\left(\frac{\beta_m-c_m}{z}+\theta_{\varpi}\right)\varepsilon\right) \tag{24}$$

$$E_{\chi}\left[z^n\right]=\sum_{k_0=1}^{\eta_m-1}\alpha_m\xi_m(k_0)\sum_{k_1=0}^{\eta_1-1}...\sum_{k_{\varpi}=0}^{\eta_{\varpi}-1}\Theta(\varpi)\sum_{r_2=0}^{2k_2-1}...\sum_{r_{\varpi}=0}^{2k_{\varpi}-1}\Omega(\varpi)\sum_{v_2=0}^{\lfloor\Lambda_2/2\rfloor}...\sum_{v_{\varpi}=0}^{\lfloor\Lambda_{\varpi}/2\rfloor}\Phi(\varpi)\frac{e^{\theta_{\varpi}\varepsilon}}{4}\Gamma\left(\frac{1}{2}\Lambda_{\varpi}+k_{\varpi}-v_{\varpi}+1\right)$$
$$\sum_{r_0=0}^{k_0-n}\binom{k_0-n}{r_0}(-\theta)^{r_0}\varepsilon^{n+0.5\Lambda_{\varpi}+k_{\varpi}-v_{\varpi}+r_0+1}\frac{\Gamma(2k_0-n-r_0+1)\Gamma(k_0+v_{\varpi}-0.5\Lambda_{\varpi}-n-r_0-k_{\varpi}-1)}{(\beta_m-c_m)^{1+k_0-n}\Gamma(k_0-n-r_0)} \tag{25}$$

Therefore, the OP of the q-th terminal in the mth beam of OTFS-based downlink non-orthogonal multiple access for high-throughput satellites is given by

$$\Pr\left\{R_{q^m}\leqslant\gamma_{q^m}\right\}=1-\mathbf{\Phi}\left(\frac{\varsigma_{q^m}-E_{\chi}(z)}{E_{\chi}(z^2)-E_{\chi}^2(z)}\right), \tag{26}$$

where $\mathbf{\Phi}(.)$ is the cumulative distribution function of the standard normally distributed RV.

B. Ergodic Capacity Analysis

The capacity analysis is an important indicator of wireless communication systems, which can guide the maximum achievable rate. The ergodic capacity is defined as the statistical mean of the instantaneous mutual information between the source and the target terminal (in bits per second per hertz). Under the statistical channel state information condition, the ergodic capacity of the q-th terminal in the m-th beam is defined as

$$\begin{aligned}\bar{C}_{q^m}&=E\left[\log_2\left(1+\mathrm{SINR}_{q^m}\right)\right]\\&=\int_0^{\infty}\log_2(1+x)\,f_{\mathrm{SINR}_{q^m}}(x)\,dx.\end{aligned} \tag{27}$$

Obviously, the exact analytic expression of (27) is not resolvable. For the convenience of representation, the SINR_{q^m} is equivalent to the RV D. Therefore, the Taylor series expansion of the logarithmic function $\log_2(1+D)$ around the mean $E[D]$ of RV D is utilized, retaining its second-order form. A closed-form approximate ergodic capacity expression is obtained, which can be given by

$$\bar{C}_{q^m}\approx\frac{\ln(1+E[D])}{\ln(2)}-\frac{E\left[D^2\right]-E^2[D]}{2\ln(2)(1+E[D])^2}. \tag{28}$$

In order to solve (28), we need to derive the closed-form expression for the moment of D. Similar to the derivation of (25), insert the PDF of D into the generalized n-th moment function to obtain (29), at the top of next page, where

$$O=-\frac{\left(P_mG_m\sum_{j=q+1}^{J_m}\xi_{j^m}+E_{\chi}[z]\right)^2}{2\left(E_{\chi}\left[z^2\right]-E_{\chi}^2[z]\right)}. \tag{30}$$

See Appendix E for the proof. Setting $n=1$ and $n=2$ in $E[D^n]$ to obtain the first and second statistical moments of D, respectively, which are substituted into (28) to obtain the ergodic capacity $\bar{C}_{q^m}$. Therefore, for all terminals within the LEO satellite coverage, the system ergodic capacity $\bar{C}$ can be given by

$$\bar{C}=\sum_{u=1}^{N_u}\sum_{j=1}^{J^u}\bar{C}_{j^u}. \tag{31}$$

V. PERFORMANCE EVALUATION

This section presents numerical results to validate the accuracy of the theoretical analysis, demonstrating the impact of key parameters on the outage probability and ergodic capacity performance, as well as the communication performance in the presence of frequency offset estimation errors.

Considering the OP performance evaluation of the OTFS-NOMA in three LEO channel with heavy shadow (HS), average shadow (AS), and light shadow (LS) fading. We simulate a Ku-band multi-beam satellite downlink communication system, serving an area that includes massive high-mobility terminals, with relative DSs ranging from 372-387 kHz [25]. Each beam selects two or three terminals out of C_u terminals to form a NOMA group, and the DD domain dimension $M=1024$, $N=14$. Table I summarizes the main parameters used in the simulation.

Figure 3 compares the OP of terminals using OTFS signal or OFDM signal in different LEO downlink channel scenarios. Setting a fixed number of beams $U=3$, and each beam is generated by 4 transmitting antennas, i.e., $N_u=4$. In one time slot, each beam selects three terminals to form a NOMA group as an example. Firstly, with the deterioration of satellite-ground channel fading, the transmitted signal suffers more severe damage, and the OP of both transmission schemes

$$E\left[D^n\right]=\frac{1}{\sqrt{2^n\pi}}(P_mG_m\xi_{q^m})^{n-2}\left(E_\chi\left[z^2\right]-E_\chi^2\left[z\right]\right)^{\frac{1-n}{2}}\left((1+(-1)^n\right)\sqrt{E_\chi\left[z^2\right]-E_\chi^2\left[z\right]}\Gamma\left(\frac{3-n}{2}\right)$$
$$_1F_1\left[\frac{n}{2}-1,\frac{1}{2},O\right]-\sqrt{2}\left(-1+(-1)^n\right)\left(P_mG_m\sum_{j=q+1}^{J_m}\xi_{j^m}+E_\chi\left[z\right]\right)\Gamma\left(2-\frac{n}{2}\right)_1F_1\left[\frac{n}{2}-1,\frac{1}{2},O\right]) \tag{29}$$

TABLE I
SYSTEM PARAMETER CONFIGURATION

Parameter	Value
Satellite orbital altitude	800 km
Satellite antenna gain	30 dB
Terminal antenna gain	$0 \sim 5$ dB
3dB-beam width of the beam	$0.5°$
Carrier frequency	15 GHz
System bandwidth	20 MHz
Satellite transmit power	40 dBW/MHz
Terminal speed	$100 \sim 300$ km/h
Number of beams U	10
Effective nadir angle $\theta_{m,u}$	$0 \sim 20°$
Heavy shadowing η, b, ω	1, 0.063, 0.0007
Average shadowing η, b, ω	5, 0.251, 0.279
Light shadowing η, b, ω	10, 0.158, 1.29

increases. Secondly, under three fading conditions, the OP of OTFS is lower than that of OFDM in the same transmit signal-to-noise ratio (SNR). The reason is that the OTFS modulation spreads the symbol to the whole TF domain instead of one OFDM symbol, and the full TF diversity is obtained. As shown in the Figure 3, the channel conditions of terminal 1 are worse than those of other terminals, because the power assigned to terminal 1 is the largest, the OP becomes the lowest. In the actual system, the power allocation needs to be optimally set according to the actual demand.

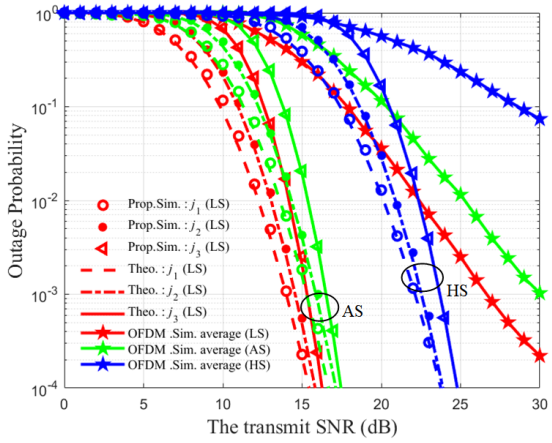

Fig. 3. OP performance comparison among OTFS-NOMA and OFDM-NOMA in different fading conditions.

Figure 4 illustrates the impact of the number of active beams on the OP of the terminals. The fixed satellite-to-ground channel is AS channel. As an example, a NOMA group contains two terminals. It can be seen that with the number of co-frequency beams increases, the terminal is subjected to more co-frequency interference, and the OP increases, which is also consistent with the rule described in Eq. (26). Specifically, the OP when activating 6 beams is slightly higher than when activating 3 beams, but significantly lower than when activating 10 beams. This is because with 10 beams, the leakage from the main lobe or the first side lobe of the newly activated adjacent beams, which are targeting the terminal, significantly increases the OP. Therefore, scheduling adjacent beams in a time slot should be avoided as much as possible. In addition, the performance of OTFS is better than the OFDM scheme in different number of active beams.

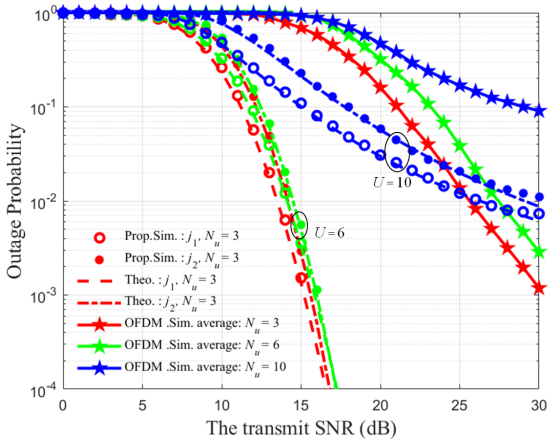

Fig. 4. OP performance comparison among OTFS-NOMA and OFDM-NOMA in different number of active beams.

Figure 5 compares the spectral efficiency of OTFS and OFDM with different number of terminals, with the horizontal axis is the transmit SNR, and the vertical axis is the normalized ergodic capacity. Maintain a constant total amount of satellite resources, including transmission power and DD domain resources. Different numbers of terminals share all communication resources. For instance, a single terminal can exclusively utilize all the resources, achieving the maximum efficiency. In cases with two or three terminals, the inevitable introduction of interference between terminals lowers efficiency, but it enables more access. The slope of each curve increases as the transmit SNR increases. In addition, compared to the OFDM scheme, the proposed framework improves performance by 16.9%, 14.3%, and 11.9% respectively when the number of terminals is $J = 1, 2, 3$ with SNR = 10.

Figure 6 further illustrates the combined impact of different numbers of active beams on OP and EC under LS channel. Specifically, subfigure (6a) shows the OP of the terminals in beam m, while subfigure (6b) shows the system EC. Use the algorithm in [22] to select three terminals in beam m. Set the fixed terminal power coefficient ξ_j, SNR = 16 dB. As shown in (6a), the OP for terminals gradually increases with the number of active beams, which is due to the introduction

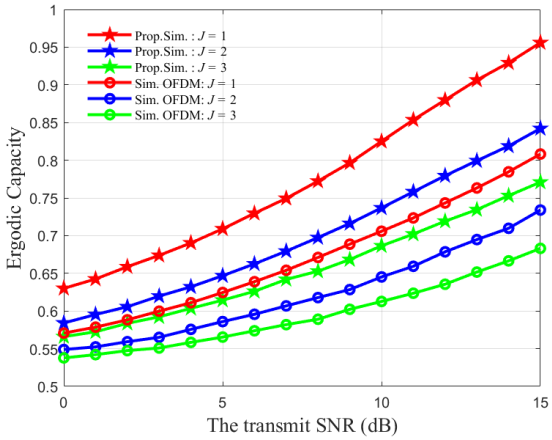

Fig. 5. The ergodic capacity comparison among OTFS-NOMA and OFDM-NOMA in different number of terminals.

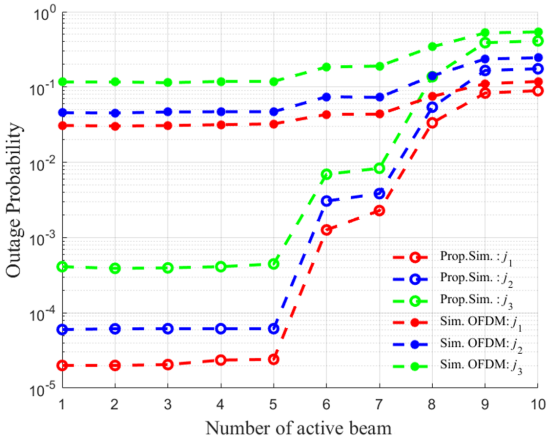

(a) The OP of terminals in beam m with SNR = 16 dB.

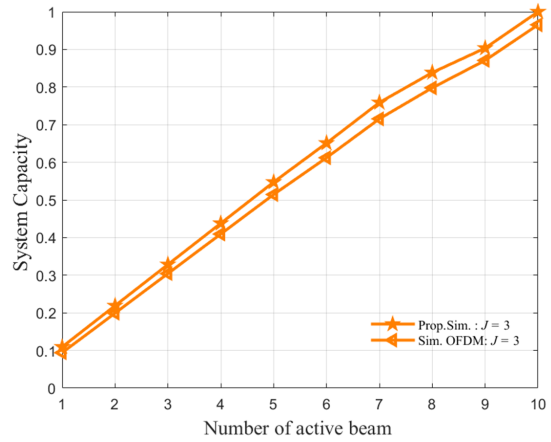

(b) The system EC with SNR = 16 dB.

Fig. 6. Comparison OP and EC performance between the the proposed framework and OFDM for different U.

of more co-frequency interference. The gentle slope indicates that the activated beams cause less interference to the beam m, whereas the steep slope indicates that beams closer to the beam m have been activated. Notably, OTFS-NOMA consistently outperforms OFDM in terms of OP under these conditions. Meanwhile, the increase in the number of activated beams allows for more terminal access, thereby providing greater system capacity, as shown in (6b). Obviously, under the premise of meeting the requirement of terminal OP, the OTFS-NOMA framework supports more terminals access, and has a larger system capacity.

Figure 7 shows the effect of Doppler grid length N on the OP of terminals. Set fixed SNR = 13 dB. As observed, when the parameter N increases, the OP for terminals utilizing the OTFS-NOMA framework gradually decreases, while the OP for terminals employing OFDM remains constant. This is beacause the full TF diversity gain offered by OTFS. As N increases, more gain is achieved. In contrast, OFDM cannot exploit the benefits beyond the scope of a single OFDM symbol. However, a larger N also corresponds to a longer frame duration, which makes it more challenging to track channel variations, thereby degrading channel estimation performance, and increasing complexity. Therefore, we need to consider the trade-off between the Doppler grid length N and implementability for practical applications.

Due to the fractional DS on OTFS in actual communication, the deviation is introduced into equalization, leading to inter-symbol interference. Figure 8 shows the impact of frequency offset estimation bias on the bit error rate (BER) of terminals, where (8a) shows the deviation present in LOS path, and (8b) shows the deviation present in NLOS path. Set $N = 14$ and the subcarrier interval to $\Delta f = 15$ kHz. In (8a), the BER performance deteriorates rapidly with the increase of LOS path deviation, because the deviation causes signal severe distortion, and destroys orthogonality. When the deviation of the LOS path reaches $\frac{\Delta f}{2N}$, the BER performance of both schemes gradually approaches 0.5. In contrast, the degradation of the proposed framework is slower. Compared to the LOS path, the NLOS path has lower power, and its deviation causes less interference on the signal, as shown in (8b). As the deviation of the NLOS path increases, the BER of both schemes rises to a fixed value, and exhibits damped oscillations. This phenomenon is caused by the interference pattern described in Chapter II.B. Specifically, the proposed OTFS-NOMA exhibits better BER performance compared to OFDM in different SNR. Additionally, to mitigate the performance degradation caused by estimation bias in practice, one can increase N to obtain greater diversity gain, while also improving Doppler resolution to reduce estimation bias.

VI. Conclusion

This paper investigates the reliability performance of an integrated OTFS-NOMA framework in multi-beam satellite downlink communication. First, we establish the signal transmission model of the proposed framework. Secondly, we derive a closed-form expression for the outage probability and ergodic capacity based on OTFS-NOMA transmission. Specifically, we derive a new expression to describe multi-beam interference with different beam gains. Unlike the complex conventional expressions, this new expression takes a simple finite sum form. Finally, we conduct performance evaluation

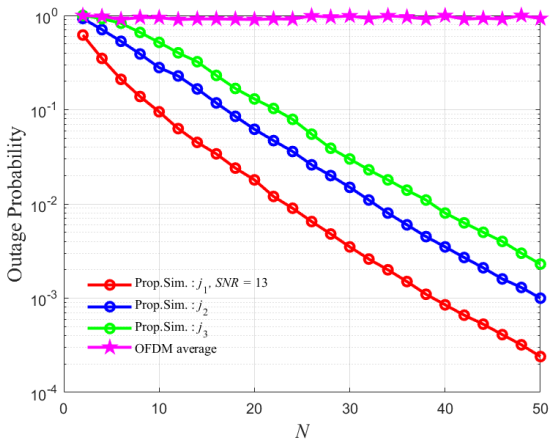

Fig. 7. The OP of terminals under different Doppler grid lengths N.

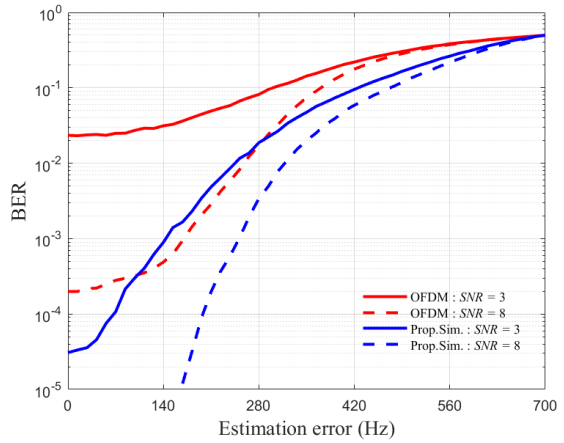

(a) The frequency offset estimation bias of LOS path, $J = 1$.

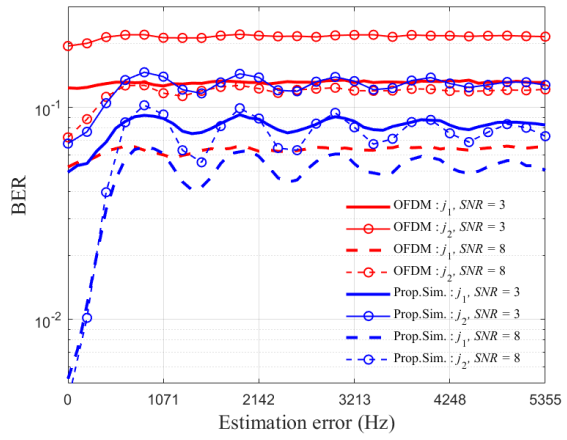

(b) The frequency offset estimation bias of NLOS path, $J = 2$.

Fig. 8. The BER comparison among OTFS-NOMA and OFDM-NOMA in different frequency offset estimation bias.

of the proposed framework, considering factors such as transmission SNR, the number of active beams, the number of terminals, DD domain configurations, and the frequency offset estimation bias. In satellite-to-ground transmission scenarios with severe DSs, our proposed framework significantly reduces the outage probability and increases system capacity by over 11.9% compared to the OFDM scheme. At the same time, we provide guidance for addressing the trade-offs among reliability improvements, capacity enhancements, and complexity in practical scenarios, which are determined by modulation size, beam scheduling, and terminal scheduling.

Appendix A
Proof the correlation of the SR distribution A_{iu}

Given that two RVs are correlated, i.e, $A_2 = kA_1, k > 0$. By combining (2), the PDF of A_2 can be given by

$$f_{A_2}(x|b_2,\omega_2,\eta_2) = \frac{1}{k} f_{A_1}\left(\frac{x}{k}\right) = \frac{x}{k^2 b_1}\left(\frac{2k^2 b_1 \eta_1}{2k^2 b_1 \eta_1 + k^2 \omega_1}\right)^{\eta_1} e^{-\frac{x^2}{2k^2 b_1}} {}_1F_1\left(\eta_1; 1; \frac{k^2 \omega_1 x^2}{2k^2 b_1 (2k^2 b_1 \eta_1 + k^2 \omega_1)}\right) \triangleq f_{A_1}\left(x|k^2 b_1, k^2 \omega_1, \eta_1\right) \tag{A.1}$$

Appendix B
Proof for equation (22)

Since $Z \triangleq Y_1 + Y_2 + \ldots Y_\varpi$, which means the transmitted signal envelope of ϖ beams is superimposed at the receiver of terminal q. First, substitute $f_{X'_u}$ into $f_{Y_u}(x) = \frac{1}{\rho_u} f_{X'_u}\left(\frac{x}{\rho_u}\right)$ to obtain the PDF of the RV Y, which can given by

$$f_{Y_u}(x) = \sum_{k_u=0}^{\eta_u - 1} \frac{\alpha_u}{\rho_u^{2k_u+2}} \xi_u(k_u)\, x^{2k_u+1} e^{-\frac{\beta_u - c_u}{\rho_u^2} x^2}. \tag{A.2}$$

To obtain the PDF of Z, utilizing the convolution theory, we first derive the PDF of sum of two i.i.d. RVs, denoted by

$$f_{Y_1+Y_2}(z) = \int_{-\infty}^{\infty} f_{Y_1}(x)\, f_{Y_2}(z-x)\, dx, z \geq 0. \tag{A.3}$$

In order to simplify the independent variables of the first term in the convolution, ρ_n is normalized, i.e. $\rho_u = \left[1, \frac{\rho_2}{\rho_1}, \ldots \frac{\rho_\varpi}{\rho_1}\right]$. Substitute (A.3) into (A.2), utilizing the binomial expansion and [26, Eq. (3.462.2)], the integral is solved as

$$f_{Y_1+Y_2}(z) = \sum_{k_1=0}^{\eta_1-1}\sum_{k_2=0}^{\eta_2-1} \frac{\alpha_1\alpha_2}{\rho_2^{2k_2+2}} \xi_1(k_1)\,\xi_2(k_2) \sum_{r_2=0}^{2k_2+1} \binom{2k_2+1}{r_2} (-1)^{r_2} \sum_{v_2=0}^{\lfloor \Lambda_2/2 \rfloor} \frac{\sqrt{\pi}\Lambda_2! \mu_2^{\Lambda_2 - 2v_2} (\mu_1+\mu_2)^{v_2 - \Lambda_2 - \frac{1}{2}}}{4^{v_2}(\Lambda_2 - 2v_2)! v_2!} z^{2k_2+2k_1-2v_2+2} e^{-\left(\frac{\mu_1\mu_2}{\mu_1+\mu_2}\right)z^2} \tag{A.4}$$

where $\Lambda_2 = 2k_1 + r_2 + 1$, $\mu_1 = \frac{\beta_1 - c_1}{\rho_1^2}$ and $\mu_2 = \frac{\beta_2 - c_2}{\rho_2^2}$.

Similarly, calculate the PDF of the sum of three i.i.d. RVs, which is given by (A.5), at the top of next page, where $\Lambda_3 = 2k_2 + 2k_1 - 2v_2 + r_3 + 2$, $\mu_3 = \frac{\beta_3 - c_3}{\rho_3^2}$. By repeating the $\varpi - 1$ times convolution operation, the closed formulation expression of PDF for ϖ RVs can be obtained, as shown in (22).

$$f_{Y_1+Y_2+Y_3}(z)=\sum_{k_1=0}^{\eta_1-1}\sum_{k_2=0}^{\eta_2-1}\sum_{k_3=0}^{\eta_3-1}\frac{\alpha_1\alpha_2\alpha_3}{\rho_2^{2k_2+2}\rho_3^{2k_3+2}}\xi_1(k_1)\,\xi_2(k_2)\,\xi_3(k_3)\sum_{r_2=0}^{2k_2+1}\sum_{r_3=0}^{2k_3+1}(-1)^{r_2+r_3}\binom{2k_2+1}{r_2}\binom{2k_3+1}{r_3}$$
$$\sum_{v_2=0}^{\lfloor\Lambda_2/2\rfloor}\sum_{v_3=0}^{\lfloor\Lambda_3/2\rfloor}\frac{\pi\Lambda_2!\Lambda_3!\mu_2{}^{\Lambda_2-2v_2}\mu_3{}^{\Lambda_3-2v_3}(\mu_1+\mu_2)^{v_2-\Lambda_2-\frac{1}{2}}\left(\frac{\mu_1\mu_2}{\mu_1+\mu_2}+\mu_3\right)^{v_3-\Lambda_3-\frac{1}{2}}}{4^{v_2+v_3}(\Lambda_2-2v_2)!(\Lambda_3-2v_3)!v_2!v_3!}z^{2k_3+2k_2+2k_1-2v_3-2v_2+3}e^{-\left(\frac{\mu_1\mu_2\mu_3}{\mu_1\mu_2+\mu_1\mu_3+\mu_2\mu_3}\right)z^2} \tag{A.5}$$

APPENDIX C
PROOF FOR EQUATION (24)

Solve the PDF of RV χ by integrating the product of Ξ and $\Psi+\varepsilon$, represented as

$$f_\chi(z)=\int_0^\infty\frac{1}{y}f_\Xi\left(\frac{z}{y}\right)f_{\Psi+\varepsilon}(y)\,dy. \tag{A.6}$$

By substituting (21) and (23) into (A.6), we can obtain

$$f_\chi(z)=\frac{1}{4}\sum_{k_0=1}^{\eta_m-1}\alpha_m\xi_m(k_0)\sum_{k_1=0}^{\eta_1-1}\cdots\sum_{k_\varpi=0}^{\eta_\varpi-1}\Theta(\varpi)\sum_{r_2=0}^{2k_2-1}\cdots\sum_{r_\varpi=0}^{2k_\varpi-1}\Omega(\varpi)$$
$$\sum_{v_2=0}^{\lfloor\Lambda_2/2\rfloor}\cdots\sum_{v_\varpi=0}^{\lfloor\Lambda_\varpi/2\rfloor}\Phi(\varpi)\,z^{-k_0-2}e^{\theta_\varpi\varepsilon}\cdot\int_\varepsilon^\infty y^{k_0+1}(y-\varepsilon)^{\frac{\Lambda_\varpi+2k_\varpi-2v_\varpi}{2}}e^{-\left(\frac{\beta_m-c_m}{z}+\theta_\varpi\right)y}dy \tag{A.7}$$

The integral part is solved by [26, Eq. (3.383.4)], and after necessary mathematical transformation, (24) is obtained.

APPENDIX D
PROOF FOR EQUATION (25)

For the nth moment of a RV χ, it is defined as

$$E_\chi[z^n]=\int_0^\infty z^n f_\chi(z)\,dz. \tag{A.8}$$

By substituting (24) into (A.8), we need to solve the integral term, which can be given by

$$\int_0^\infty\left(\frac{\beta_m-c_m}{z}+\theta_\varpi\right)^{-\frac{\Lambda_\varpi+2k_\varpi+2k_0-2v_\varpi+6}{4}}W_{\frac{2k_0-\Lambda_\varpi-2k_\varpi+2v_\varpi+2}{4},-\frac{2k_0+\Lambda_\varpi+2k_\varpi-2v_\varpi+4}{4}}\left(\left(\frac{\beta_m-c_m}{z}+\theta_\varpi\right)\varepsilon\right)\frac{e^{-\frac{\left(\frac{\beta_m-c_m}{z}+\theta_\varpi\right)\varepsilon}{2}}}{z^{2-n+k_0}}dz \tag{A.9}$$

Next, replace the variable with $\left(\frac{\beta_m-c_m}{z}+\theta_\varpi\right)\varepsilon\rightarrow t$, utilizing [26, Eq. (7.621.11)] and the binomial expansion, we can obtain

$$\sum_{r_0=0}^{k_0-n}\binom{k_0-n}{r_0}(-\theta)^{r_0}(\beta_m-c_m)^{n-k_0-1}\varepsilon^{\frac{4n+4r_0+\Lambda_\varpi+2k_\varpi-2k_0-2v_\varpi+2}{4}}\Gamma(2k_0-n-r_0+1)\cdot\frac{\Gamma(k_0-n-r_0-0.5\Lambda_\varpi-k_\varpi+v_\varpi-1)}{\Gamma(k_0-n-r_0)},k_0\geqslant n+r_0 \tag{A.10}$$

The equation (25) is obtained after sorting.

APPENDIX E
PROOF FOR EQUATION (29)

Since (25) obtains the distribution characteristics of $\sum_{\kappa'=0}^{N-1}\sum_{\iota'=0}^{M-1}\chi(\kappa',\iota')$ using moment matching. Therefore, the n-th moment of D can be expressed as

$$E[D^n]=\int_{-\infty}^\infty x^n f_D(x)\,dx, \tag{A.11}$$

where $f_D(.)$ is the PDF of D. Utilizing Jacobian transformations and mathematical transformations, the function is denoted by

$$f_D(x)=\frac{P_mG_m\xi_{q^m}}{x^2\sqrt{2\pi\left(E_\chi[z^2]-E_\chi^2[z^1]\right)}}\exp\left(-\frac{\left(\frac{P_mG_m\xi_{q^m}}{x}-P_mG_m\sum_{j=q+1}^{J_m}\xi_{j^m}-E_\chi[z^1]\right)^2}{2\left(E_\chi[z^2]-E_\chi^2[z^1]\right)}\right). \tag{A.12}$$

By substituting (A.12) in (A.11), and solve the integral, (29) is obtained after sorting.

REFERENCES

[1] L. Lei, A. Wang, E. Lagunas, X. Hu, Z. Zhang, Z. Wei, and S. Chatzinotas, "Spatial-temporal resource optimization for uneven-traffic LEO satellite systems: Beam pattern selection and user scheduling," *IEEE Journal on Selected Areas in Communications*, vol. 42, no. 5, pp. 1279–1291, 2024.

[2] M. Giordani and M. Zorzi, "Non-terrestrial networks in the 6G era: Challenges and opportunities," *IEEE Network*, vol. 35, no. 2, pp. 244–251, 2021.

[3] T. Hwang, C. Yang, G. Wu, S. Li, and G. Ye Li, "OFDM and its wireless applications: A survey," *IEEE Transactions on Vehicular Technology*, vol. 58, no. 4, pp. 1673–1694, 2009.

[4] R. Hadani, S. Rakib, M. Tsatsanis, A. Monk, A. J. Goldsmith, A. F. Molisch, and R. Calderbank, "Orthogonal time frequency space modulation," in *2017 IEEE Wireless Communications and Networking Conference (WCNC)*, 2017, pp. 1–6.

[5] S. K. Mohammed, "Derivation of OTFS modulation from first principles," *IEEE Transactions on Vehicular Technology*, vol. 70, no. 8, pp. 7619–7636, 2021.

[6] H. B. Mishra, P. Singh, A. K. Prasad, and R. Budhiraja, "OTFS channel estimation and data detection designs with superimposed pilots," *IEEE Transactions on Wireless Communications*, vol. 21, no. 4, pp. 2258–2274, 2022.

[7] Y. Liu, S. Zhang, F. Gao, J. Ma, and X. Wang, "Uplink-aided high mobility downlink channel estimation over massive MIMO-OTFS system," *IEEE Journal on Selected Areas in Communications*, vol. 38, no. 9, pp. 1994–2009, 2020.

[8] Z. Wei, S. Li, W. Yuan, R. Schober, and G. Caire, "Orthogonal time frequency space modulationpart i: Fundamentals and challenges ahead," *IEEE Communications Letters*, vol. 27, no. 1, pp. 4–8, 2023.

[9] S. Li, W. Yuan, Z. Wei, R. Schober, and G. Caire, "Orthogonal time frequency space modulationpart ii: Transceiver designs," *IEEE Communications Letters*, vol. 27, no. 1, pp. 9–13, 2023.

[10] W. Yuan, Z. Wei, S. Li, R. Schober, and G. Caire, "Orthogonal time frequency space modulationpart iii: Isac and potential applications," *IEEE Communications Letters*, vol. 27, no. 1, pp. 14–18, 2023.

[11] J. Shi, Z. Li, J. Hu, Z. Tie, S. Li, W. Liang, and Z. Ding, "OTFS enabled LEO satellite communications: A promising solution to severe doppler effects," *IEEE Network*, vol. 38, no. 1, pp. 203–209, 2024.

[12] X. Wang, W. Shen, C. Xing, J. An, and L. Hanzo, "Joint bayesian channel estimation and data detection for OTFS systems in LEO satellite communications," *IEEE Transactions on Communications*, vol. 70, no. 7, pp. 4386–4399, 2022.

[13] S. Li, M. Zhang, C. Ju, D. Wang, W. Chen, P. Zhou, and D. Wang, "Downlink carrier frequency offset estimation for OTFS-based LEO satellite communication system," *IEEE Communications Letters*, vol. 28, no. 1, pp. 163–167, 2024.

[14] S. K. Devarajalu and D. Jose, "Performance evaluation of OTFS under different channel conditions for LEO satellite downlink," in *2023 10th International Conference on Wireless Networks and Mobile Communications (WINCOM)*, 2023, pp. 1–6.

[15] J. Hu, J. Shi, S. Ma, and Z. Li, "Secrecy analysis for orthogonal time frequency space scheme based uplink LEO satellite communication," *IEEE Wireless Communications Letters*, vol. 10, no. 8, pp. 1623–1627, 2021.

[16] J. Shi, J. Hu, Y. Yue, X. Xue, W. Liang, and Z. Li, "Outage probability for OTFS based downlink LEO satellite communication," *IEEE Transactions on Vehicular Technology*, vol. 71, no. 3, pp. 3355–3360, 2022.

[17] C. Xu, L. Xiang, J. An, C. Dong, S. Sugiura, R. G. Maunder, L.-L. Yang, and L. Hanzo, "OTFS-aided ris-assisted SAGIN systems outperform their OFDM counterparts in doubly selective high-doppler scenarios," *IEEE Internet of Things Journal*, vol. 10, no. 1, pp. 682–703, 2023.

[18] Z. Ding, R. Schober, P. Fan, and H. Vincent Poor, "OTFS-NOMA: An efficient approach for exploiting heterogenous user mobility profiles," *IEEE Transactions on Communications*, vol. 67, no. 11, pp. 7950–7965, 2019.

[19] X. Zhou, K. Ying, Z. Gao, Y. Wu, Z. Xiao, S. Chatzinotas, J. Yuan, and B. Ottersten, "Active terminal identification, channel estimation, and signal detection for grant-free NOMA-OTFS in LEO satellite internet-of-things," *IEEE Transactions on Wireless Communications*, vol. 22, no. 4, pp. 2847–2866, 2023.

[20] Y. Ma, G. Ma, N. Wang, Z. Zhong, J. Yuan, and B. Ai, "Enabling OTFS-TSMA for smart railways mMTC over LEO satellite: A differential doppler shift perspective," *IEEE Internet of Things Journal*, vol. 10, no. 6, pp. 4799–4814, 2023.

[21] A. Abdi, W. Lau, M.-S. Alouini, and M. Kaveh, "A new simple model for land mobile satellite channels: first- and second-order statistics," *IEEE Transactions on Wireless Communications*, vol. 2, no. 3, pp. 519–528, 2003.

[22] M. Abdelfatah, A. Zekry, and S. ElSayed, "User selection methods for overcoming growing number of served users in massive mimo systems," *IEEE Access*, vol. 11, pp. 59 981–59 994, 2023.

[23] G. Zheng, S. Chatzinotas, and B. Ottersten, "Generic optimization of linear precoding in multibeam satellite systems," *IEEE Transactions on Wireless Communications*, vol. 11, no. 6, pp. 2308–2320, 2012.

[24] N. I. Miridakis, D. D. Vergados, and A. Michalas, "Dual-hop communication over a satellite relay and shadowed rician channels," *IEEE Transactions on Vehicular Technology*, vol. 64, no. 9, pp. 4031–4040, 2015.

[25] T. S. Kelso, "Analysis of the Iridium 33-Cosmos 2251 collision," *Adv. Astronautical Sci.*, vol. 135, pp. 1009–1112, 2009.

[26] I. S. Gradshteyn and I. M. Ryzhik, *Table of integrals, series, and products*, 7th ed. San Diego, CA, USA: Academic, 2007.